Electronic Supplementary Material (ESI) for ChemComm.

Structure and thermal expansion of the distorted Prussian blue analogue $RbCuCo(CN)_6$

SUPPLEMENTARY INFORMATION

Hanna L. B. Boström[a,b*] and Ronald I. Smith[c]

[a] Department of Chemistry, Ångström Laboratory, Uppsala University, Box 538, 751 21 Uppsala, Sweden.

[b] Department of Chemistry, University of Oxford, Inorganic Chemistry Laboratory, South Parks Road, Oxford OX1 3QR, UK.

[c] ISIS Facility, Rutherford Appleton Laboratory, Harwell Campus, Didcot OX11 0QX, UK.

*To whom correspondence should be addressed; E-mail: hanna.bostrom@kemi.uu.se

Contents

1 Experimental details

Energy-dispersive X-ray spectroscopy

The metal ratio was confirmed by energy-dispersive X-ray spectroscopy in a Zeiss Merlin scanning electron microscope equipped with an Ultim Max 100 mm^2 Silicon Drift Detector. The data were acquired using an acceleration voltage of 20 kV and a beam current of 1 nA for 20 min at a working distance of 6.0 mm. The data was evaluated using the AZtec software and light elements (C, N and O) were included in the fit to the spectra. A minimum of 12 positions were measured for each of the 5 samples, giving an average composition as shown in Table S1. Representative morphology is shown in Fig. S1.

Table S1: Composition as determined by EDX

Metal	Ratio
Rb	0.90(9)
Cu	1
Co	0.92(6)

Thermogravimetric analysis

Thermometric analysis was carried out under N_2 gas using a Perkin Elmer thermogravimetric analyzer TGA 7. The sample was held at 30 °C for 15 min followed by heating at 5 °C min^{-1} until 500 °C. The sample mass as a function of temperature is shown in Fig. S2. Assuming the mass loss until ∼250 °C to be water loss gives an estimated water content of 3–5 water molecules per formula unit. Note that this calculation will also include surface-adsorbed water.

Powder diffraction

Powder X-ray diffraction was carried out on the I11 beamline at Diamond Light Source, UK, using a beam energy of 15 keV. The data were collected using the Mythen2 PSD detector with short exposure times (2×4 s, 0.25 ° offset) to prevent significant beam damage to the samples. A Si NIST 640c standard standard was measured to obtain accurate instrument parameters

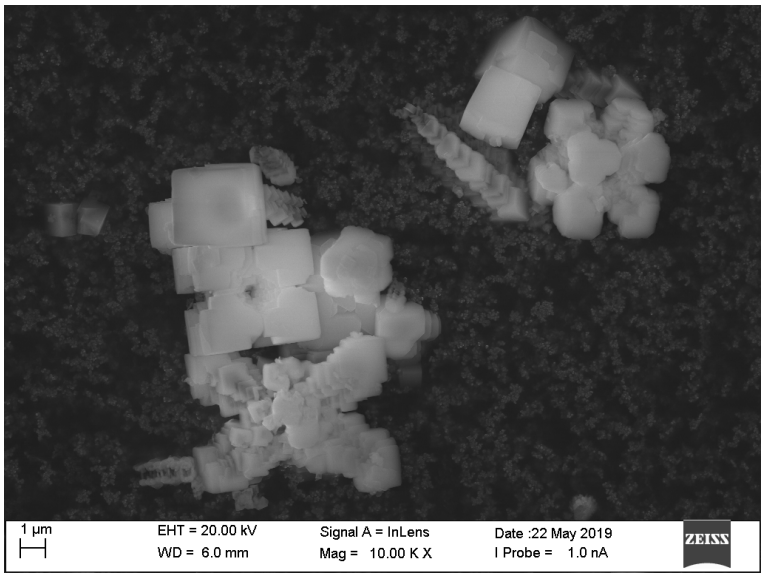

Figure S1: Representative morphology of $RbCuCo(CN)_6$

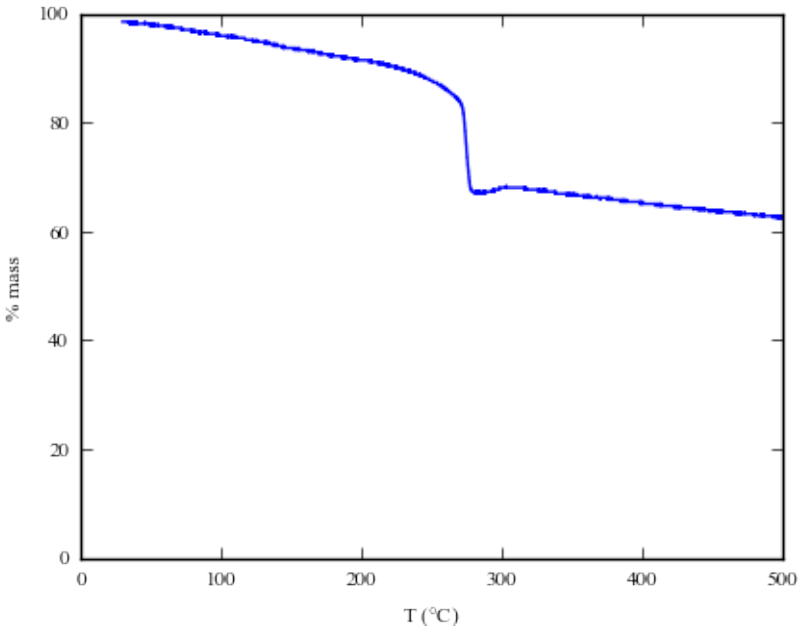

Figure S2: Thermogravimetric analysis of $RbCuCo(CN)_6$

(*i.e.* intrinsic peak shape, wavelength and zero point). Additional strain terms were added to the refinement to adjust the model peak shape to fit the data. Variable-temperature diffraction

patterns were collected in the range 100–500 K on heating using an Oxford cryostream. To prevent beam damage, the sample was translated between successive measurements to ensure irradiation of a pristine part.

Time-of-flight neutron powder diffraction patterns (NPD) were collected on the GEM instrument[S1] at the ISIS neutron and muon source, Rutherford Appleton Laboratory, UK. The sample ($\sim$ 600 mg) was dehydrated in vacuum at 120 °C for 24 h prior to loading into a 6 mm vanadium sample can and sealed with indium wire. Data were collected at room temperature for 350 μAh integrated proton beam current to the ISIS target, corresponding to an exposure time of approximately 2 hours in the neutron beam. Initial data manipulation and reduction was carried out using the Mantid software package.[S2, S3]

Crystal structure refinement was performed using the Topas software[S4, S5] with data from detector banks 2–6 and average 2θ angles 17.9486–153.898°. Structural parametrisation in terms of distortion modes was obtained from ISODISTORT.[S6] The background was modelled by a Chebyshev polynomial function. The occupancies were restrained to the values obtained by EDX and the distribution of Rb over the two independent sites was refined. No distance restraints were applied. Anisotropic displacement parameters were allowed to vary within ±50% of the isotropic value and certain off-diagonal terms in the tensor were fixed to 0 to avoid unphysical displacements.

2 Crystallographic details

Table S2: Crystallographic details determined by neutron powder diffraction for $RbCuCo(CN)_6$ at ambient conditions.

Space group	$Cccm$
a /Å	10.86045(24)
b /Å	9.98193(29)
c /Å	10.03977(25)
V /Å^3	1088.394(48)
Z	4
R_{wp}	6.412%

Atom	occ	x	y	z	u_{11}	u_{22}	u_{33}	u_{12}
Cu	1	0.25	0.75	0	0.0303(50)	0.030(10)	0.0101(82)	0.0067(62)
Co	0.92	0.25	0.25	0	0.030(17)	0.030(33)	0.010(26)	0.004(19)
C	0.92	0.42642(90)	0.22613(76)	0	0.0180(42)	0.0180(54)	0.0060(41)	−0.0110(50)
C	0.92	0.25	0.25	0.8104(11)	0.0180(51)	0.0060(63)	0.0060(58)	−0.0056(42)
C	0.92	0.25224(76)	0.44414(90)	0	0.0180(53)	0.0060(55)	0.0060(54)	0
N	0.92	0.53017(71)	0.20357(56)	0	0.0431(53)	0.0431(47)	0.0144(33)	0.0085(40)
N	0.92	0.25	0.25	0.69701(90)	0.0431(47)	0.0144(52)	0.0144(51)	0.0053(34)
N	0.92	0.78701(56)	0.05449(71)	0	0.0431(51)	0.0144(46)	0.0144(46)	−0.0074(34)
Rb	0.8305(92)	0	0.5	0.25	0.089(10)	0.0463(81)	0.0302(75)	0
Rb	0.0695(92)	0	0	0.25	0.09(13)	0.030(84)	0.030(94)	0

Table S3: Variable-temperature lattice parameters of $RbCuCo(CN)_6$, as found from Pawley refinements of powder X-ray diffraction data.

T / K	a / Å	b / Å	c / Å
100	10.79625(11)	9.96713(10)	10.04184(10)
150	10.81295(11)	9.96845(10)	10.03961(9)
200	10.83505(11)	9.97263(10)	10.03945(9)
250	10.85033(11)	9.97232(9)	10.03616(9)
300	10.86868(11)	9.97441(9)	10.03498(9)
350	10.8875(2)	9.9784(2)	10.03627(14)
400	10.9008(2)	9.97948(14)	10.03499(14)
450	10.9155(2)	9.9821(2)	10.0351(2)
500	10.9320(2)	9.9841(2)	10.0349(2)

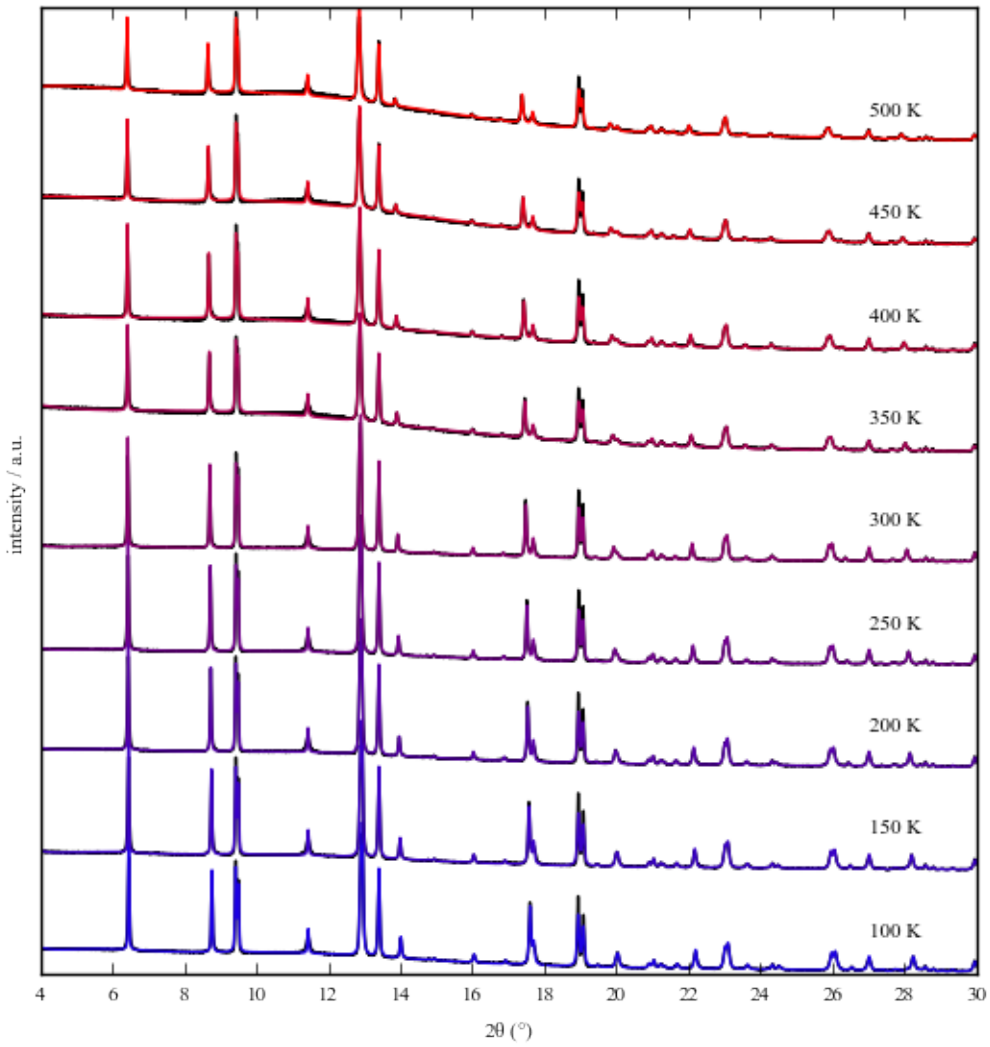

Figure S3: Variable-temperature X-ray diffraction patterns of $RbCuCo(CN)_6$ (black) with the simulated patterns from Pawley refinements (blue to red).

3 Group-theoretical discussion

For primitive cubic systems (parent space group $Pm\bar{3}m$), the accessible zone-boundary irreducible representations (irreps) are described by the letters R ($\frac{1}{2}$, $\frac{1}{2}$, $\frac{1}{2}$), M ($\frac{1}{2}$, $\frac{1}{2}$, 0) and X ($\frac{1}{2}$, 0, 0) and the zone-centre irrep by Γ (0, 0, 0). The coordinates in brackets give the propagation

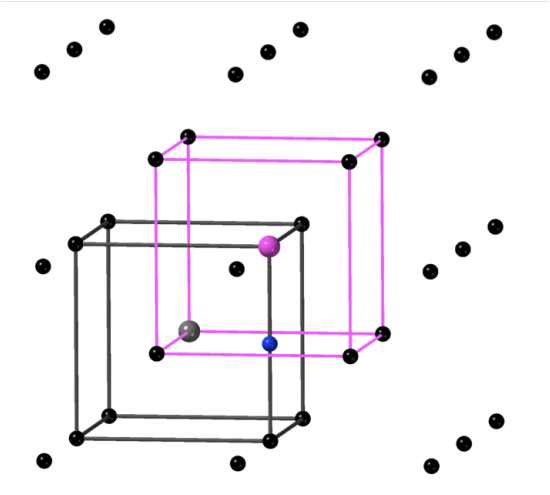

Figure S4: The reciprocal unit cell of a face-centred cubic cell is body-centred cubic, as shown. For the cell drawn in black, the blue point corresponds to ($\frac{1}{2}$, $\frac{1}{2}$, 0) relative to the central grey lattice point. Following a translation to the (equally valid) unit cell in purple with a purple central lattice point, the blue point is now described by the coordinates (0, 0, $\frac{1}{2}$) relative to the purple lattice point. Hence, these two sets of coordinates refer to the same point in reciprocal space.

vector/wavevector of the distortion. Distortions with different periodicities necessarily transform as distinct irreps and so are distinguishable by symmetry. As an example, the conventional tilt systems of a simple perovskite are described by R_4^+ (out-of-phase) and M_3^+ (in-phase).[S7] Molecular perovskites also support unconventional tilting[S8, S9] transforming as one of Γ_4^+, X_3^+, X_5^+, or M_5^+ (see Ref. 10 for visual depictions). Note that the irrep R_1^+ corresponds to B-site cation order and thus results in the double perovskite structure with space group $Fm\bar{3}m$.

In face-centred cubic systems (parent space group $Fm\bar{3}m$), the characters of the X- and M-type distortions—with respect to the primitive structure—mix [Fig. S4]. In other words, these points in reciprocal space (periodicities in real space) are now indistinguishable by symmetry and are both referred to by X. To illustrate, the conventional in-phase tilt system $a^0a^0c^+$ gives the symmetry $P4/mbm$ when acting on the $Pm\bar{3}m$ parent (irrep M_3^+).[S7, S11] The unconventional tilt described by X_3^+ yields $P4/mcc$, which is easily distinguishable from $P4/mbm$ by virtue of the glide planes. However, when these two tilt systems are present in double perovskites with parent symmetry $Fm\bar{3}m$, the space group $P4/mnc$ is obtained in *both* cases. The irrep relative to the $Fm\bar{3}m$ parent is X_3^+ for both of these tilts.

It is possible to map pairs of irreps with respect to $Pm\bar{3}m$ to the corresponding irreps in $Fm\bar{3}m$, by evaluating the combined effect of each irrep with respect to $Pm\bar{3}m$ with the "face-centring mode" R_1^+. Such analysis is readily performed using the group-theoretical software ISODISTORT[S6] and the results are given in Table S4. The distortion modes on the same row have identical symmetry-breaking properties when acting upon the $Fm\bar{3}m$ aristotype. In two cases (where the irrep is described by k_2^-), there is a direct mapping between the irrep labels in $Fm\bar{3}m$ and $Pm\bar{3}m$ and the inclusion of R_1^+ has no effect.

Γ-point modes do not lead to superlattice reflections in diffraction measurements and their detection can be challenging. A familiar example are magnetic structures, where antiferromagnetic spin order induces additional reflections in neutron diffraction patterns, whereas ferromagnetic order does not. Distortions that transform as R-point modes in $Pm\bar{3}m$—*e.g* out-of-phase tilting and certain orbital order patterns—appear at the Γ-point relative to $Fm\bar{3}m$, as seen in Table 1. As a result, the Jahn-Teller distortion described by R_4^+ gives additional reflections when acting on the primitive ABX_3 $Pm\bar{3}m$ aristotype, but not when it appears in double perovskites ($Fm\bar{3}m$ aristotype), as it is now a Γ mode. This Jahn-Teller distortion is therefore more difficult to probe in double perovskite relative to simple perovskites. A related example of this problem occurs in A-site ordered 1322 perovskites, such as $NaMn_7O_{12}$.[S12] Here, the R-point orbital order relative to $Pm\bar{3}m$ transforms as a Γ-point mode relative to the $Im\bar{3}m$ aristotype and hence requires detailed neutron diffraction to detect.[S13]

Table S4: The relationship between distortions in $Pm\bar{3}m$ and $Fm\bar{3}m$. Irreps are given for the structure with the B-site at the origin.

$Fm\bar{3}m$		$Pm\bar{3}m$			
Irrep	Space group	Irrep	Distortion	Irrep	Distortion
Γ_1^+	$Fm\bar{3}m$	Γ_1^+	cubic strain	R_1^+	B-site order
Γ_3^+	$I4/mmm$	Γ_3^+	tetragonal strain	R_3^+	Jahn-Teller distortion
Γ_4^+	$I4/m$	Γ_4^+	unconventional tilt	R_4^+	conventional tilt
Γ_5^+	$Immm$	Γ_5^+	orthorhombic strain	R_5^+	A-site displacement
Γ_2^-	$F\bar{4}3m$			R_2^-	A-site order
Γ_4^-	$I4mm$	Γ_4^-	polar mode	R_4^-	polar mode
Γ_5^-	$I\bar{4}2m$	Γ_5^-	octahedral deformation	R_5^-	octahedral deformation
X_1^+	$P4/mmm$	X_1^+	B-site order	M_1^+	B-site order
X_2^+	$P4_2/mnm$	X_2^+	Jahn-Teller distortion	M_2^+	Jahn-Teller distortion
X_3^+	$P4/mnc$	X_3^+	unconventional tilt	M_3^+	conventional tilt
X_4^+	$P4_2/mmc$	X_4^+	octahedral deformation	M_4^+	A-site order
X_5^+	$Cmce$	X_5^+	unconventional tilt	M_5^+	unconventional tilt
X_2^-	$P4_2/nmc$			M_2^-	A-site displacement
X_3^-	$P4/nmm$	X_3^-	A-site order	M_3^-	columnar shift
X_4^-	$P4_2/nnm$	X_4^-	octahedral deformation	M_4^-	octahedral deformation
X_5^-	$Cmcm$	X_5^-	columnar shift	M_5^-	antipolar mode

4 References

(S1) W. G. Williams, R. M. Ibberson, P. Day and J. E. Enderby, *Physica B*, 1998, **241–243**, 234–236.

(S2) O. Arnold, J. C. Bilheux, J. M. Borreguero, A. Buts, S. I. Campbell, L. Chapon, M. Doucet, N. Draper, R. Ferraz Leal, M. A. Gigg, V. E. Lynch, A. J. Markvardsen, D. J. Mikkelson, R. L. Mikkelson, R. Miller, K. Palmen, P. Parker, G. Passos, T. G. Perring, P. F. Peterson, S. Ren, M. A. Reuter, A. T. Savici, J. W. Taylor, R. J. Taylor,

R. Tolchenov, W. Zhou and J. Zikovsky, *Nucl. Instrum. Methods Phys. Res., Sect. A*, 2014, **764**, 156–166.

(S3) *Mantid (2013): Manipulation and Analysis Toolkit for Instrument Data.; Mantid Project. http://dx.doi.org/10.5286/SOFTWARE/MANTID*.

(S4) H. M. Rietveld, *Acta Crystallogr.*, 1967, **22**, 151–152.

(S5) A. A. Coelho, *TOPAS-Academic, version 4.1 (computer software)*, Coelho Software, Brisbane.

(S6) B. J. Campbell, H. T. Stokes, D. E. Tanner and D. M. Hatch, *J. Appl. Cryst.*, 2006, **39**, 607–614.

(S7) C. J. Howard and H. T. Stokes, *Acta Crystallogr. B Struct. Sci.*, 1998, **54**, 782–789.

(S8) S. G. Duyker, J. A. Hill, C. J. Howard and A. L. Goodwin, *J. Am. Chem. Soc.*, 2016, **138**, 11121–11123.

(S9) J. A. Hill, A. L. Thompson and A. L. Goodwin, *J. Am. Chem. Soc.*, 2016, **138**, 5886–5896.

(S10) H. L. B. Boström, M. S. Senn and A. L. Goodwin, *Nat. Commun.*, 2018, **9**, 2380.

(S11) A. M. Glazer, *Acta Crystallogr. B Struct. Cryst. Cryst. Chem.*, 1972, **28**, 3384–3392.

(S12) M. Marezio, P. D. Dernier, J. Chenavas and J. C. Joubert, *J. Solid State Electrochem.*, 1973, **6**, 16–20.

(S13) A. Prodi, E. Gliolo, A. Gauzzi, F. Licci, M. Marezio, F. Bolzoni, Q. Huang, A. Santoro and J. W. Lynn, *Nat. Mater.*, 2004, **3**, 48–52.